minerals

MDPI

Article

The Effect of the Emeishan Mantle Plume on the Genetic Mechanism of the Maokou Formation Reservoir in the Central Sichuan Region

Qimin Guo [1], Xizhe Li [1,2,*], Zhenhua Guo [1], Lin Zhang [1], Mao Zhu [3], Mengfei Zhou [2], Yize Huang [2], Xiangyang Pei [1], Yunlong Wu [4], Wen Li [5], Mengnan Yan [5], Shan Du [6] and Hongming Zhan [1,2,*]

1 PetroChina Research Institute of Petroleum Exploration and Development, Beijing 100083, China; guoqimin123@petrochina.com.cn (Q.G.); guozhenhua@petrochina.com.cn (Z.G.); zl69@petrochina.com.cn (L.Z.); peixy@petrochina.com.cn (X.P.)
2 School of Engineering Science, University of Chinese Academy of Sciences, Beijing 100049, China; zhoumengfei19@mails.ucas.ac.cn (M.Z.); yize.huang@psu.edu (Y.H.)
3 PetroChina Hangzhou Research Institute of Geology, Hangzhou 310023, China; zhum_hz@petrochina.com.cn
4 Exploration and Development Research Institute of PetroChina Daqing Oilfield Co., Ltd., Daqing 163712, China; wuyunlongyjy@petrochina.com.cn
5 Exploration and Development Research Institute, PetroChina Southwest Oil & Gasfield Company, Chengdu 610041, China; liwensk@petrochina.com.cn (W.L.); yanmengnan96@petrochina.com.cn (M.Y.)
6 Exploration and Development Research Institute of Huabei Oilfield Company, Renqiu 062552, China; yjy_ds@petrochina.com.cn
* Correspondence: lxz69@petrochina.com.cn (X.L.); zhanhongming17@mails.ucas.ac.cn (H.Z.)

Abstract: Thin layers and high-yield dolomite reservoirs were recently discovered in the Permian Guadeloupian Maokou Formation. The genetic mechanism of this reservoir is controversial because of its complex sedimentation and diagenesis in the Maokou Formation. Traditionally, the genesis has focused on sedimentation, karst, and fracture, whereas the influence of the Emeishan mantle plume activity (EMP) has been ignored. In this study, we enumerated petrographic (grouped into micritic bioclastic limestone, limy dolomite, grain dolomite, dolomite cement, calcite cement, and saddle dolomite) and geochemical data ($\delta^{13}C$, $\delta^{18}O$, REE, and $^{87}Sr/^{86}Sr$) from a microscopic perspective to support the impact of EMP on reservoirs. We conclude that EMP activity altered the sedimentary environment and induced a complex diagenesis. The paleogeomorphic reconstruction data indicate that the EMP caused an uplift zone in the NE–SW direction, depositing advantageous high-energy beach facies. In terms of diagenesis, the abnormally high $^{87}Sr/^{86}Sr$ ratios and REE with positive Eu anomalies suggest that dolomitization was influenced by both seawater and hydrothermal fluids. Based on the above evidence, we established a reservoir genetic model for the Maokou Formation related to the intensity of the EMP. This study provides a new perspective on the mantle plume activity for the study of carbonate reservoir genesis.

Keywords: Emeishan mantle plume; central Sichuan Basin; Maokou Formation; genetic model

Citation: Guo, Q.; Li, X.; Guo, Z.; Zhang, L.; Zhu, M.; Zhou, M.; Huang, Y.; Pei, X.; Wu, Y.; Li, W.; et al. The Effect of the Emeishan Mantle Plume on the Genetic Mechanism of the Maokou Formation Reservoir in the Central Sichuan Region. *Minerals* **2024**, *14*, 129. https://doi.org/10.3390/min14020129

Academic Editors: Jan Golonka, Vahid Tavakoli and Hamzeh Mehrabi

Received: 27 November 2023
Revised: 13 January 2024
Accepted: 16 January 2024
Published: 24 January 2024

1. Introduction

The Sichuan Basin occupies a significant position in global oil and gas exploration because of its extensive resources, diverse reservoir types, and complex geological structures [1–3]. Reservoirs in the Permian Maokou Formation in the central Sichuan Basin have attracted considerable attention because of their high-yield gas flows and complex genetic mechanisms. The Maokou Formation reservoir in the central Sichuan Basin comprises thin-layered dolomite within limestone strata; as such, it is unique because its composition differs significantly from reservoirs in other areas [4–9]. There are multiple explanations for the genesis mechanism of this special reservoir, which can be divided into two categories:

sedimentary genesis and diagenetic genesis [10–12]. With sedimentary genesis, the reservoir is controlled mainly by the distribution of intermediate to high-energy beach facies within the platform [13–16]. Diagenetic genesis can be further divided into two categories according to whether the reservoir is controlled by karstification or fracture distribution. With the former, a thin-layer reservoir is formed by interstratal karst caused by the leaching effect of meteoric water [17–20]. With the latter, the reservoir is mainly a type controlled by fracture distribution, based on evidence of highly developed fractures that are filled or semi-filled with saddle dolomite in the core [21–23]. There is also a composite genesis of sedimentation and karst jointly controlling reservoirs [24–26]. But most of the causal mechanisms only focus on a specific factor, ignoring the underlying cause of the Emeishan mantle plume (EMP) activity.

The sedimentary and early diagenesis stage (~271–260 Ma) of the Maokou Formation occurred earlier than that of the Emeishan large igneous province (ELIP, ~260 Ma), accompanied by EMP activity [27–29]. Owing to the temporal coupling relationship between the EMP activity and the development of the Maokou Formation, it is considered that all factors relating to reservoir genesis (including sedimentation, karst, faults) are related to this intense geological activity. And there have been reports that the EMP activity has changed the sedimentary environment, leading to uplift and karst processes, on a large scale across the entire Sichuan Basin [30–32]. Therefore, the genesis of the Maokou Formation reservoir is likely to be controlled by the EMP activity.

To verify this hypothesis, we conducted research from both sedimentary and diagenetic perspectives, investigating the changes in the sedimentary environment through core descriptions, paleogeomorphic reconstruction and the important diagenesis in reservoir formation based on petrologic and geochemical analyses. The reservoir genesis mechanism influenced by EMP is established. And the results and conclusion provide guidance for the exploration and development of carbonate gas reservoirs and provide a new perspective on the mantle plume activity for the study of carbonate reservoir genesis.

2. Geological Setting

The study region (30°10′29″ N, 106°15′18″ E) is located in the Sichuan Basin, which is superimposed on the Upper Yangtze Block and has experienced multiple tectonic movements and complex later reformation [33–36]. The basin is divided into six secondary tectonic units (Figure 1B): the gentle tectonic belt in central Sichuan where the study region is located, the high, steep fold belt in eastern Sichuan, the low, steep fold belt in western Sichuan, the gentle tectonic belt in southwestern Sichuan, the low, steep fold belt in southern Sichuan, and the gentle tectonic belt in northern Sichuan [37].

2.1. EMP Activity and the ELIP

The ELIP is the only large igneous province recognized by the international academic community in China owing to continuous arching and EMP activity. The ELIP occurred between the Guadalupian and Lopingian at ~260 Ma [38–41]. The range of erupted basalt covers 7×10^5 km^2 [42] and is mainly restricted to the junction between Yunnan, Sichuan, and Guizhou provinces in the southern Sichuan Basin [43–46]. The basalt erupted unconformably on the limestone strata of the Maokou Formation, and its thickness gradually decreased from the southwest to northeast of the Sichuan Basin [47,48]. The ELIP caused climate change [49,50] and was associated with the Permian–Triassic (P-T) mass extinction event [51–55].

The mantle plume hypothesis has been widely adopted to explain the origins of large igneous provinces, and sedimentologic, geophysical, and geochemical evidence has proven that the ELIP was caused by EMP activity [56–58]. Mantle plume activity is a process in which high-temperature material arches up causing the crust to uplift and rupture, and the high-temperature material finally erupts to form basalt [59–63]. Based on differences in the degree of erosion around the ELIP center, the eroded zones can be divided into three parts: inner, middle, and outer zones [64] (Figure 1A). The Sichuan Basin is located in the outer

zone of the ELIP, but previous studies have also reported basalt outcrops in this area [41], indicating that EMP activity also had a significant effect on reservoirs in the central Sichuan Basin. The Maokou Formation has undergone varying degrees of erosion owing to the influence of EMP activity.

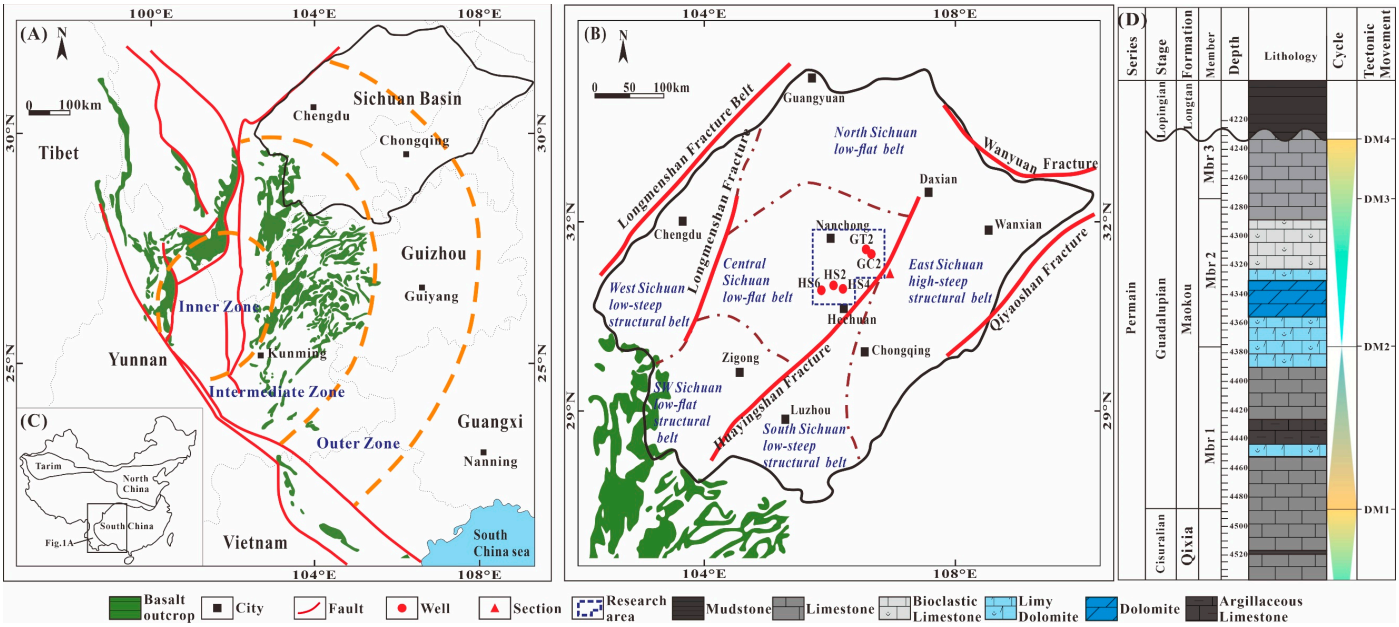

Figure 1. (**A**) Distribution of the Emeishan Large Igneous Province (ELIP) [64]. According to the magnitude of strata uplift and erosion, the ELIP can be divided into the inner, intermediate, and outer zones. (**B**) Location of the study area and tectonic units; (**C**) location of Sichuan Basin; (**D**) stratigraphic column of the Maokou Formation (Permian) in the central Sichuan Basin. In the study area, Mbr4 has been eroded, leaving Mbr1, Mbr2, and Mbr3. There is unconformity contact between Mbr3 and the Longtan Formation.

The Sichuan Basin has undergone a series of tectonic movements throughout its geological history. The Dongwu Movement (DM) occurred in the Middle Permian, related to EMP activity [65,66]. The DM significantly influenced the sedimentation and early diagenesis of the Maokou Formation reservoir. The DM was a multiphase movement, and many division schemes have been proposed for its active stages [67–72]. The latest proposed scheme divides the DM into four stages [73], and these are related to the development of the Maokou Formation as follows: The first stage (DM1) occurred at the beginning of the deposition of the Mbr 1, characterized by local uplift of the strata and relative sea level decline. The second stage (DM2) occurred between the deposition of Mbr 2 and Mbr 3, characterized by continuous uplift and the formation of local plateaus, leading to differentiation of sedimentary environments. The third stage (DM3) occurred after the deposition of Mbr 4, which directly led to erosion and loss of Mbr 4, and the fourth stage (DM4) was accompanied by the ELIP, where faults generated by the tectonic movement provided channels for the upward migration of basalt. Based on EMP activity and these four most recently defined stages of the DM, this study provides further evidence of the causal relationship between the EMP and the formation of Maokou Formation reservoirs. In addition, the main controlling factors and formation models of Maokou Formation reservoirs are investigated.

2.2. Stratigraphy and Depositional Setting

After a long hiatus in the Late Carboniferous–Early Permian, a large-scale transgression occurred in the Upper Yangtze region during the Kungurian; this was followed by a steady decrease in sea level, transitioning from coal-bearing clastic shore facies to carbonate platform facies [74]. Under this depositional setting, the Maokou Formation

was deposited in the Middle Permian, which conformably overlies the Qixia Formation and unconformably underlies the Longtan Formation, and it has an estimated age of 270–260 Ma [75]. The Maokou Formation can be divided into four lithological members from top to bottom, with Mbr 1 to Mbr 3 being a depositional cycle and Mbr 4 being another one. Mbr 4 in most areas of the Sichuan Basin is missing due to the influence of the Dongwu Movement. In the late stage of the Middle Permian Maokou Formation, the strata were up-lifted and eroded, resulting in the unconformity of the Longtan Formation shale covering Mbr 3 in the study area [13,17].

Mbr 1 is a transgressive systems tract (TST). During this period, the Sichuan Ba-sin experienced a major transgression process, and the paleogeomorphology still showed a trend of high in the west and low in the east. The seawater in the basin gradually became shallower from east to west. This period was the highest sea level of the Lower Permian and lasted for a long time, with relatively low sea water energy and mostly developed gentle slope facies. The Mbr 1 sediment is mainly composed of dark gray and grayish black mudstone and layered micritic bioclastic limestone. Layered limestone exhibits undulating features, forming eyelids and eyeball shaped limestone. Paleontology is characterized by the Cryptospirifer brachiopod fauna. Mbr 2 to Mbr 3 form a high-stand systems tract (HST). During this period, the seawater in the basin has gradually receded from west to east, marking the lowest relative sea level period of the Maokou Formation. At this time, the seawater energy is relatively high, and the main sedimentary facies is the open platform facies. Mbr2 is mainly composed of bioclastic limestone and dolomite, with gray dolomite developed between the limestone and dolomite. Mbr 3 is mainly composed of light-gray clastic limestone. During the sedimentation process of Mbr 3, the sea level gradually increased, and the energy of seawater decreased.

3. Materials and Methods

From a macro perspective, the residual thickness method and impression method were used to reconstruct the paleogeomorphology. The restoration of paleogeomorphology mainly relies on geological thickness data. Due to the marine invasion during the Mbr 1 sedimentary period, the restoration of paleogeomorphology in the Qixia Formation was carried out using the impression method, utilizing the stratigraphic thickness data of Mbr 1. The residual thickness method is used to restore the paleogeomorphology of Mbr 2, mainly utilizing the sedimentary thickness data of Mbr3.

Based on the above macro-analysis, 16 samples were selected in different paleogeomorphological positions within drill cores from Wells HS2, HS4, and HS6, and dolomite, limestone, and cement samples were collected and used for microscopic analysis and testing.

Thin sections were impregnated with blue epoxy to highlight porosity and stained with Alizarin Red S to conduct a detailed petrographic study. All samples were washed with distilled water, dried overnight to ensure purity, extracted with a dental drill, and ground to <200 mesh using an agate mortar [76]. All geochemical experiments and analyses ($\delta^{13}C$ and $\delta^{18}O$, $^{87}Sr/^{86}Sr$, trace earth elements) were performed at the Key Laboratory of Carbonate Reservoir, China National Petroleum Corporation.

To conduct $\delta^{13}C$ and $\delta^{18}O$ analyses, ~200–300 μg of powder was reacted with 105% H_3PO_4 at 50 °C for 4 h, and the CO_2 produced was measured using a DELTA V Advantage isotope ratio mass spectrometer coupled to Gasbench II. The $\delta^{13}C$ and $\delta^{18}O$ values were calculated relative to the Vienna Pee Belemnite scale. Under analysis precision monitoring with the NBS-19 standard and two internal standards of GBW04405 and GBW04406, the standard deviation of $\delta^{13}C$ and the $\delta^{18}O$ were found to be better than ±0.1‰ and ±0.2‰, respectively.

For the Sr isotope analysis, 50–100 mg of powder was dissolved in 1 mL HNO_3 in a Teflon container for 48 h at 190 °C. Sr was extracted from the supernatant using a conventional ion-exchange program and an ion-exchange resin. $^{87}Sr/^{86}Sr$ analyses were performed using a Triton Plus thermal ionization mass spectrometer calibrated using

the estimated SRM-987 standard. The average error of the $^{87}Sr/^{86}Sr$ ratio was a mere $\pm 0.5 \times 10^{-5}$ (2σ).

For the trace elements analyses, ~40 mg of power was dissolved in 5 mL HNO_3 in a Teflon container and dried. Another 5 mL HNO_3 (1.42 g/mL) was then added to the container for 3 h at 130 °C to remove the effects of aluminum silicates and other contaminants. Trace earth elements were analyzed using inductively coupled plasma mass spectrometry (ICP-MS). All REE concentrations were standardized using PAAS [77,78]. In this study, Ce anomalies were calculated using the following formula [79,80]:

$$Ce/Ce^* = Ce_N/(Pr_N \times Pr_N/Nd_N) \quad (1)$$

La anomalies were calculated using the formula [79,80]

$$La/La^* = La_N/(Pr_N \times (Pr_N/Nd_N)^2) \quad (2)$$

and Eu anomalies were calculated using the formula

$$Eu/Eu^* = Eu_N/(Sm_N^* 2/3 + Tb_N^* 1/3) \quad (3)$$

This was used to calculate the Eu anomalies ($Eu/Eu^* > 1$ indicates a positive anomaly related to hydrothermal processes) [81,82].

4. Results

4.1. Petrography

An interpretation of the logging data shows that the Maokou Formation reservoir segment in the central Sichuan region is mainly concentrated in Mbr 2 of the Maokou Formation. According to the size, distribution, and surface shape of crystals, the lithology can be divided into six types (Figure 2). The matrix rocks can be divided into two categories: limestone and dolomite. Most of the limestone is micritic bioclastic limestone (LIM) which is rich in bioclast. Dolomite can be further divided into limy dolomite (LD) and grain dolomite (GD) based on the difference in its degree of dolomitization. The types of cement can be divided into saddle dolomite (SD), dolomite cement (DC), and calcite cement (CAL). All types of cement have medium to coarse crystals which are larger than matrix rocks. Among them, there is a curved surface crystal shaped SD. The details of these six types of lithology are provided below.

LIM: All seven LIM hand specimens were light-gray and black. Bubbles were generated violently after dropping 5% HCL. Examination under an optical polarizing microscope showed large amounts of biological debris within the limestone (Figure 2A). The main matrix type of LIM is mainly micritic matrix, indicating that it was formed in a deep-water sedimentary environment with weak water energy. There are few intergranular pores. Spatially, LIM was widely distributed above and below the dolomite layer, which is the primary lithological component of the Maokou Formation.

LD (Figure 2B): The two LD hand specimens were grayish black, darker than the limestone, and they showed weak blistering after dropping 5% HCL. Microscopic thin-section observations indicated that the lithology mostly comprised fine-medium crystal GD with some calcite particles that turned red when stained with Alizarin Red S. Most of the LD develops in Mbr 2, which is the shallowest stage of the Maokou Formation seawater and has strong water energy. LD is mainly developed in the transitional zone between the limestone and dolomite layers.

GD: GD is the main lithology of the Maokou Formation reservoir, and its color is gray-black and darker than the other components. Thin-section identification showed that it was mainly composed of fine-to-medium crystal dolomite particles (Figure 2C). Compared with LD, the GD was completely dolomitized. Similar to LD, GD mainly develops in Mbr 2 and is also deposited in high-energy and shallow environments. The GD is concentrated within the thin dolomite reservoir of the Maokou Formation.

DC: DC exists in the fissures generated in GD, and no reaction was observed after dropping 5% HCL. Under a polarizing microscope, the DC particles were seen to be significantly larger than the surrounding GD, and they mainly comprised medium coarse crystal particles (Figure 2D), which would have formed during diagenesis. Cross polarization showed that the dolomite particles were relatively straight, and there was no undulating extinction (Figure 2E); therefore, they were not of a hydrothermal origin.

SD: SD is a typical hydrothermal mineral [83]. Core observations revealed that large amounts of SD were filled or semi-filled in fissures and holes developed in GD. The curved crystal shape of SD was observed in the hand specimen. Under a polarizing microscope, the saddle-shaped dolomite grains were observed to be mainly macrocrystalline particles, and they were larger than the DC and accompanied by an asphalt filling (Figure 2F). Undulating extinction characteristics were observed using an orthogonal polarizer (Figure 2G).

CAL: Unlike SD and DC, CAL was seen to exist mainly in limestone fractures (Figure 2H). During thin section observations, fine-to-medium crystal particles and coarse crystal particles were seen within the CAL. In the orthogonally polarized image, fine-medium crystal horse-tooth CAL is seen at the edge of the sample; this represents early filling, while the macrocrystalline particles in the middle of the CAL represent later filling (Figure 2I).

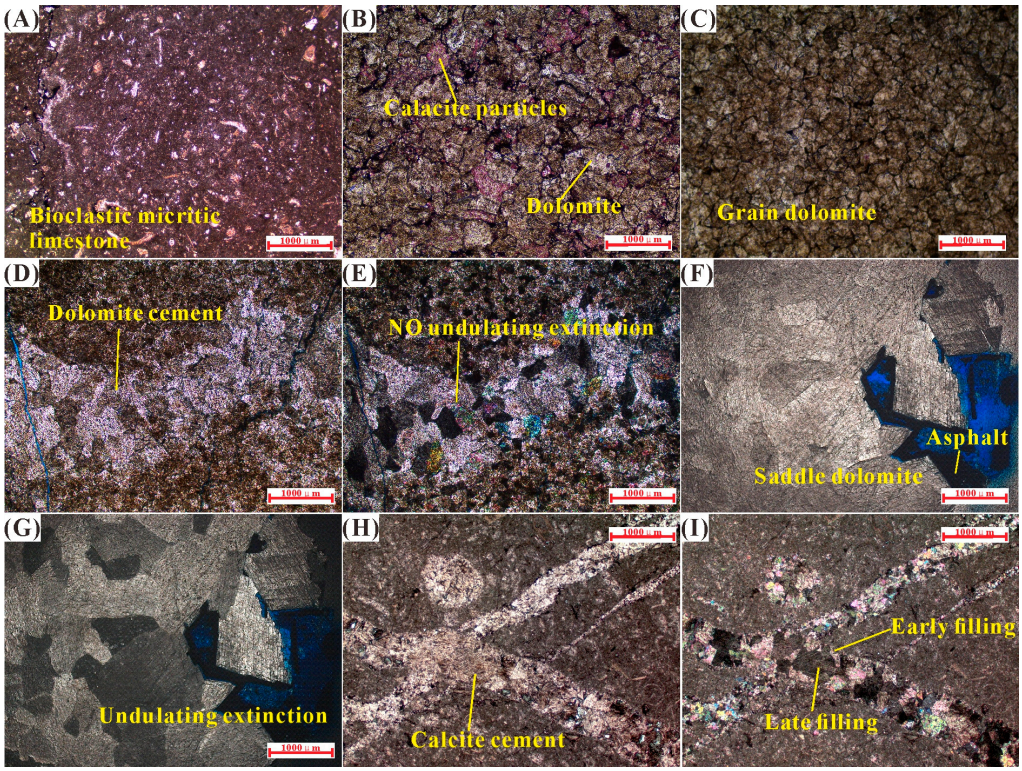

Figure 2. Photographs showing petrographic characteristics. (**A**) Microphotograph of LIM (HS4-4331.95 m); (**B**) microphotograph of LD: light red particles are calcite stained by Alizarin Red S; gray-white particles are dolomite particles (HS4-4335.20 m); (**C**) microphotograph of GD (HS4-4337.85 m); (**D**) microphotograph of DC: white band is a dolomite cement vein, and the grey is grain dolomite surrounding rock (HS4-4337.15 m); (**E**) crossed polarized microphotograph of Figure 3 (**D**). The DC has no undulating extinction characteristics and is therefore not related to a hydrothermal genesis. (**F**) Microphotograph of SD: asphalt exists between coarse particles and pores (HS6-4539.3 m); (**G**) crossed polarized microphotograph of Figure 3 (**F**). The SD has undulating extinction, which represents a hydrothermal genesis. (**H**) Microphotograph of CAL: the gray–white bands and clumps are calcite cements, and the dark gray parts are limestone surrounding rock (HS2-4334.03 m); (**I**) crossed polarized microphotograph of Figure 3 (**H**). Tooth-shaped fine particles exist at the edge of the vein (related to early filling) and coarse crystal particles exist in the middle of the vein (late filling).

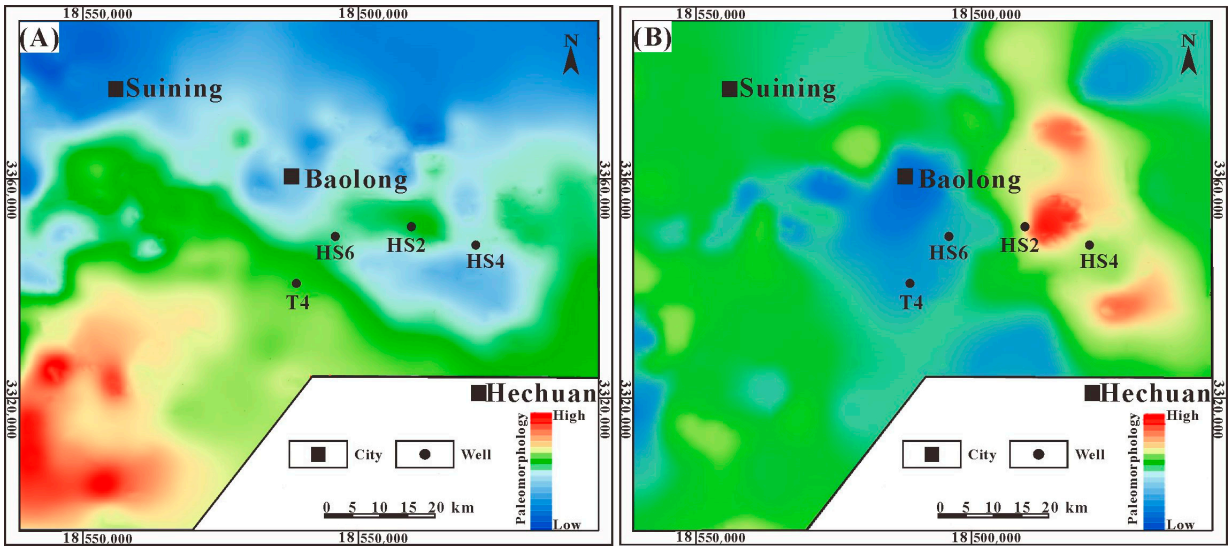

Figure 3. Reconstruction of paleogeomorphology indicating that paleogeomorphological transformation was caused by the activity of EMP. (**A**) Paleogeomorphology of the end of the Qixia Formation; (**B**) paleogeomorphology of the second member of the Maokou Formation.

4.2. Geochemistry

4.2.1. Stable Carbon and Oxygen Isotopes

The $\delta^{18}O$ distribution range within the Maokou Formation is generally negative compared with that of Permian seawater [84] (Table 1). The $\delta^{13}C$ values of LIM ranged from 1.58‰ to 4.53‰ (average 3.51‰), while the $\delta^{18}O$ isotope values ranged from −6.54‰ to −8.14‰ (average −7.20‰). The $\delta^{13}C$ values of GD spanned from 3.41‰ to 4.06‰ (average 3.86‰), and the $\delta^{18}O$ values ranged from −5.44‰ to −8.18‰ (average −7.53‰). For LD, the $\delta^{13}C$ values were from 4.07‰ to 4.10‰ (average 4.08‰), and the $\delta^{18}O$ values were from −7.60‰ to −7.64‰ (average −7.62‰). Only one sample was extracted from SD, and the $\delta^{13}C$ and $\delta^{18}O$ values were 5.05‰ and −7.62‰, respectively.

Table 1. Isotope data ($\delta^{13}C$, $\delta^{18}O$, and $^{87}Sr/^{86}Sr$) of micritic bioclastic limestone (LIM), limy dolomite (LD), grain dolomite (GD), and saddle dolomite (SD) from the Maokou Formation in the central Sichuan Basin.

Sample ID	Well	Lithology	$\delta^{18}O_{PDB}$‰	$\delta^{13}C_{PDB}$‰	$^{87}Sr/^{86}Sr$	Elemental Analysis		
						Sr/ppm	Mn/ppm	Mn/Sr
4527	HS2	LIM	−6.74	3.85	0.707317	389.98	61.94	0.16
4531	HS2	LIM	−7.77	4.04	0.707231	352.66	80.33	0.23
4533	HS2	LIM	−6.54	1.58	0.707015	368.06	123.94	0.34
4543	HS4	LIM	−8.14	4.53	0.707266	422.83	43.03	0.10
4545	HS4	LIM	−7.92	4.24	0.707330	518.31	47.57	0.09
4547	HS4	LIM	−6.54	2.64	0.707178	384.35	121.95	0.32
2028	HS6	LIM	−6.82	3.66	0.707362	473.70	10.10	0.02
4548	HS4	LD	−7.60	4.10	0.707380	222.66	92.75	0.41
4549	HS4	LD	−7.64	4.07	0.707324	281.64	78.71	0.28
4550	HS4	GD	−7.42	3.87	0.707676	133.34	170.08	1.27
4551	HS4	GD	−5.44	3.41	0.707264	746.21	23.39	0.03
2024	HS6	GD	−8.13	4.06	0.707696	84.94	31.27	0.37
2025	HS6	GD	−7.91	4.03	0.707953	65.57	31.21	0.47
2026	HS6	GD	−8.12	3.89	0.707908	68.52	40.73	0.59
2029	HS6	GD	−8.18	3.88	0.707879	66.30	31.44	0.47
2027	HS6	SD	−7.62	5.05	0.708225	120.00	48.11	0.40

4.2.2. Radiogenic Sr Isotopes

The $^{87}Sr/^{86}Sr$ ratios of the lithologies examined within the Maokou Formation were abnormally high (Table 1). The $^{87}Sr/^{86}Sr$ ratios of LIM and LD ranged from 0.707015 to 0.707362 and 0.70732 to 0.70738, respectively; therefore, the values of both LIM and LD lie within the approximate $^{87}Sr/^{86}Sr$ ratio range for Permian seawater (0.70680–0.70807) [84]. However, the $^{87}Sr/^{86}Sr$ ratios of GD were abnormally high. The $^{87}Sr/^{86}Sr$ ratio of the GD ranged from 0.707264 to 0.70908. In addition, the SD value of SD was 0.708225, which is abnormally located in the range of Permian seawater.

4.2.3. Trace Earth Elements

The highest Sr concentrations in the study areas were observed in LIM (352.67–518.31 ppm, average 415.70 ppm), compared with those of GD (65.57–746.21 ppm, average 194.14 ppm) and LD (222.67–281.65 ppm, average 252.15 ppm) (Table 1). The manganese (Mn) contents of LIM were 10.10–123.94 ppm (average 69.84 ppm) and slightly higher than those of GD (23.39–170.08 ppm, average 54.68) but lower than those of LD (78.71–92.75 ppm, average 85.73). The ratios of Mn to strontium (Sr) were characterized by ranking according to the degree of dolomitization as follows: LIM (0.02–0.33, average 0.17) < LD (0.27–0.41, average 0.34) < GD (0.03–1.27, average 0.53). The REE concentrations in different samples are presented in Table 2, and the post-Archean Australian shale (PAAS) [77]. The REE patterns of LIM were similar to those of LD, and they exhibited a seawater-like profile with enriched heavy REEs (HREEs). GD showed two REE pattern types: one was similar to LIM and LD with negative Eu anomalies (Eu/Eu*: 0.84–0.90), and the other had positive Eu anomalies (Eu/Eu*: 1.03–1.5).

Table 2. Rare earth element (REE) abundance of micritic bioclastic limestone (LIM), limy dolomite (LD), grain dolomite (GD), and saddle dolomite (SD) from the Maokou Formation in the central Sichuan Basin.

ID	Well	Lithology	La	Ce	Pr	Nd	Sm	Eu	Gd	Tb	Dy	Ho	Er	Tm	Yb	Lu	Eu/Eu*
4527	HS2	LIM	0.00569	0.00459	0.00481	0.00476	0.00554	0.00491	0.0069	0.00605	0.0063	0.00775	0.00804	0.00861	0.00748	0.00777	0.85992
4531	HS2	LIM	0.00856	0.00656	0.00767	0.00771	0.00943	0.00924	0.01363	0.01346	0.01408	0.01557	0.01671	0.0181	0.01578	0.01658	0.85866
4533	HS2	LIM	0.00775	0.00519	0.00569	0.00612	0.0066	0.0087	0.01147	0.01083	0.01221	0.01473	0.01513	0.01588	0.01328	0.0136	1.08843
4543	HS4	LIM	0.00509	0.0045	0.00468	0.00467	0.00559	0.00578	0.00667	0.00617	0.00682	0.00731	0.0084	0.00924	0.00781	0.0078	0.99944
4545	HS4	LIM	0.01847	0.01744	0.0188	0.01882	0.02456	0.02382	0.02893	0.02829	0.02959	0.03231	0.03406	0.03871	0.03394	0.03548	0.92358
4547	HS4	LIM	0.01281	0.01134	0.01209	0.01164	0.01353	0.01271	0.01589	0.01543	0.01698	0.01784	0.01937	0.01965	0.01896	0.02048	0.89775
2028	HS6	LIM	0.01345	0.0118	0.01249	0.01222	0.01469	0.01574	0.01694	0.0151	0.01494	0.01728	0.01836	0.01768	0.01482	0.01638	1.06161
4548	HS4	LD	0.01451	0.01296	0.01389	0.0136	0.01586	0.01446	0.01908	0.01757	0.0184	0.02096	0.02266	0.02582	0.02404	0.02438	0.88046
4549	HS4	LD	0.02168	0.01972	0.02008	0.01921	0.02292	0.0228	0.02608	0.02609	0.02734	0.02999	0.0294	0.03314	0.02836	0.03063	0.95138
4550	HS4	GD	0.02281	0.0206	0.02246	0.02181	0.02527	0.02198	0.0287	0.02722	0.02952	0.03142	0.03515	0.03841	0.03498	0.03741	0.84796
4551	HS4	GD	0.01967	0.02041	0.02088	0.02019	0.02233	0.02221	0.01974	0.01733	0.01623	0.01566	0.01602	0.01793	0.01601	0.01626	1.07405
2024	HS6	GD	0.01392	0.00902	0.00857	0.00739	0.00673	0.01111	0.00857	0.00877	0.00933	0.01013	0.01174	0.01366	0.01168	0.01257	1.50055
2025	HS6	GD	0.0048	0.00455	0.00484	0.00501	0.00629	0.0061	0.00815	0.00772	0.00846	0.00989	0.01161	0.01298	0.01168	0.00975	0.9017
2026	HS6	GD	0.00648	0.00562	0.00586	0.00576	0.00624	0.00716	0.00835	0.0084	0.00819	0.01005	0.01067	0.0115	0.01081	0.0096	1.03051
2029	HS6	GD	0.01425	0.01021	0.00941	0.00824	0.00797	0.009	0.00934	0.00919	0.00969	0.01034	0.01284	0.01367	0.01099	0.01222	1.07478
2027	HS6	SD	0.0108	0.0093	0.01021	0.01068	0.01177	0.01224	0.01335	0.01406	0.0146	0.01806	0.01837	0.01589	0.01579	0.01461	0.97714

5. Discussion

5.1. EMP Activity Altered the Sedimentary Environment

The most salient manifestation of EMP activity is a dome-shaped uplift on the Earth's surface [85–88] that subsequently triggered robust tectonic movements. Crustal uplift occurred globally before the eruption of the five major igneous provinces of the Emeishan (260 Ma), Siberia (251 Ma), Deccan (65 Ma), North Atlantic (161 Ma, 255 Ma), and Yellowstone (26 Ma) [89–94].

The paleogeomorphological construction conducted in this study showed that strong uplift occurred between the end of Qixia Formation development and the sedimentary stage of Mbr 2 of the Maokou Formation, and this altered the sedimentary environment and facies. During the sedimentary stage of the Qixia Formation, the paleogeomorphology was characterized by high values in the southwest and low values in the northeast in the study area (Figure 3A), whereas a NW-SE uplift zone was formed in the study area during the sedimentary stage of Mbr 2 of the Maokou Formation (Figure 3B). In the stratigraphic thickness section (Figure 4), it was also found that the sedimentary thickness of Mbr3 is thinner in the uplift zone, indicating that there was a local differential uplift in the late stage of sedimentation in Mbr 2. Differential uplift refers to the varying degrees of uplift in different regions, which determines the distribution of sedimentary environments and facies.

The changes in Paleogeomorphology caused by EMP activities lead to changes in the sedimentary environment and differential distribution of sedimentary facies (Figure 5A). Due to the formation of the NW-SE uplift zone, the originally deep-water sedimentary environment in the study area has changed to a shallow water sedimentary environment, and seawater energy has also increased from weak to strong.

In the uplift zone and its surrounding areas, high-energy beach facies are formed based on shallow water and strong energy. This sedimentary facies mainly develops limestone composed of fine-medium crystalline particles, and after varying degrees of dolomitization, LD (Figure 2B) and GD (Figure 2C) are formed, which are also identification indicators of this type of sedimentary facies. In addition, there are more abundant intergranular pores in this type of sedimentary facies (Figure 5B), which is beneficial for the development of reservoirs. The gentle slopes and depressions far away from the uplift zone have deep-water and low-energy environments. There are gentle slope and low-energy beach facies extending outward in the uplift zone and its surrounding areas. Although these facies zones are also beach facies, the energy of seawater is relatively weakened, and the sediment type changes to fine crystalline particles, with relatively fewer intergranular pores (Figure 5C). The main sedimentary facies developed in the depression are intertidal marine facies, which mainly consist of mud crystal bioclastic LIM (Figure 2A) with a micritic matrix, and there are almost no intergranular pores. Overall, the high-energy beach facies that developed in the slope zone owing to the EMP uplift formed the material basis for the development of high-quality reservoirs.

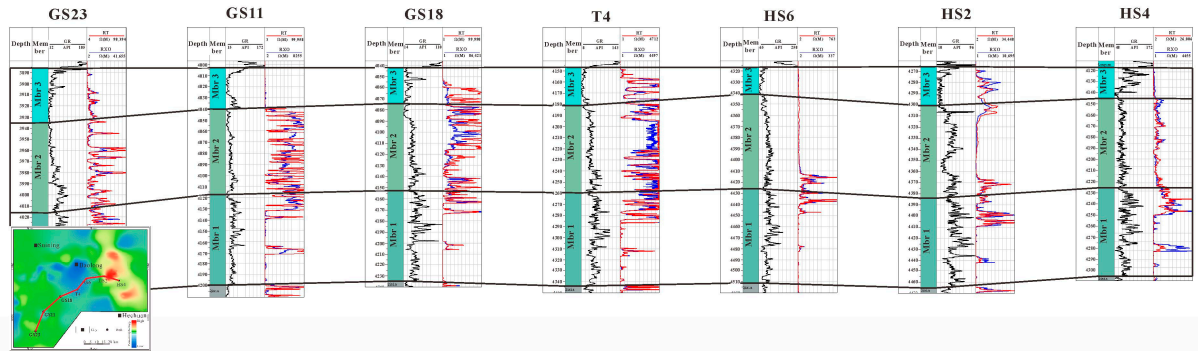

Figure 4. Comparison of stratigraphic thickness of the Maokou Formation in the Middle Permian.

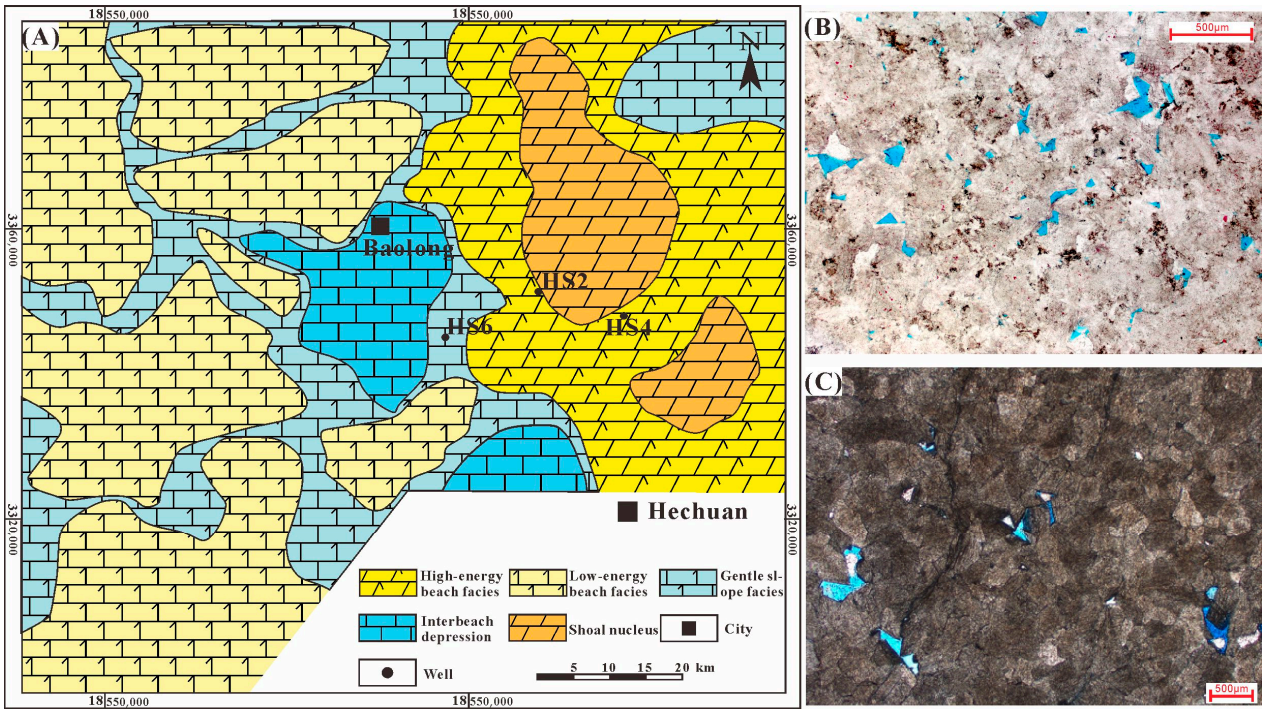

Figure 5. (**A**) Sedimentary facies distribution map of Mbr 2 of the Maokou Formation in the central Sichuan region; (**B**) microphotograph of GD, which is representative of a high-energy beach facies with abundant intergranular pores and was obtained from well of HS4 (4339.70 m); (**C**) microphotograph of GD, which is representative of gentle slope facies with low energy and poor intergranular pores and was obtained from well HS6 (4539.30 m). The comparison between (**B**,**C**) proves that high-energy sedimentary facies contain comparatively more intergranular pores.

5.2. Complex Diagenesis Resulting from EMP Activity

5.2.1. Abnormally High Geothermal Temperature

Mantle plume activity is an important heat loss mechanism that occurs in relation to energy being released from the Earth's interior [95,96]. Numerical simulations have been conducted to understand the thermal structure, heat loss, and recovery of the basalt melting temperature of mantle plumes [97–99]. There is also geochemical evidence that EMP activity caused abnormal geothermal temperatures, such as that relating to the decarbonization reaction, which resulted in sharp $\delta^{13}C$ decreases in the Maokou Formation [32]. In addition, vitrinite reflectance studies have estimated that the abnormal geothermal gradient caused by EMP activity reached 43 °C/km [100,101].

In this study, we provide two types of evidence for the abnormally high ground temperature caused by the EMP. In this respect, we first refer to a section of basalt in contact with the Maokou Formation in the Huaying area within the eastern part of the study area (Figure 6). Obvious baking and crushing phenomena are observed near the contact surface between the basalt and the Maokou Formation, indicating that the Maokou Formation experienced abnormally high thermal effects in the study area and that the reservoir of the Maokou Formation was strongly influenced by EMP activity. Second, based on the $\delta^{13}C$ and $\delta^{18}O$ data obtained from cores HS2, HS4, and HS6 in this study, and those obtained from GC2, GT2, and T4 in previous studies [18,21,22,102,103], we determined the existence of strong negative $\delta^{18}O$ values in the Maokou Formation (Figure 7A) compared to global Guadalupian seawater. This negative feature was caused by thermal fractionation accompanied by high temperatures. In addition, the degree of negative bias in LIM, GD, and SD was observed to gradually increase, thereby indicating that abnormally high geothermal temperatures existed during both the sedimentary and shallow burial periods. Furthermore, a value of $\delta^{18}O < -10\%$ in an SD sample indicated the influence of diagenetic alteration.

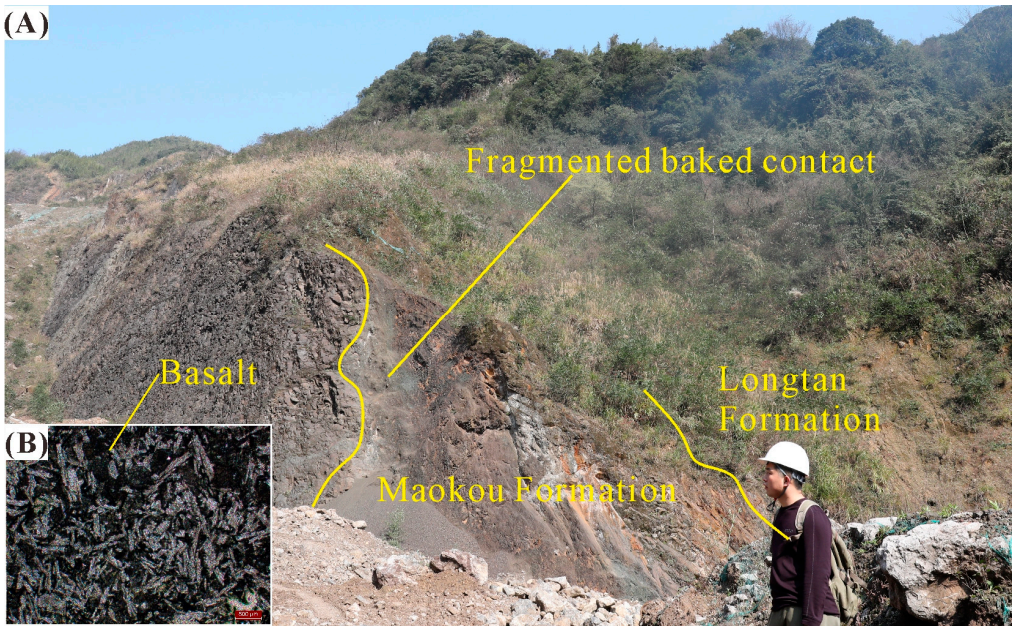

Figure 6. Photograph of Huangkongcao section. (**A**) Fragmented baked contact is observed between the basalt and the Maokou Formation, which indicates that the Maokou Formation experienced abnormally high thermal effects. The location of the profile is shown in Figure 1B. (**B**) Microphotograph of basalt.

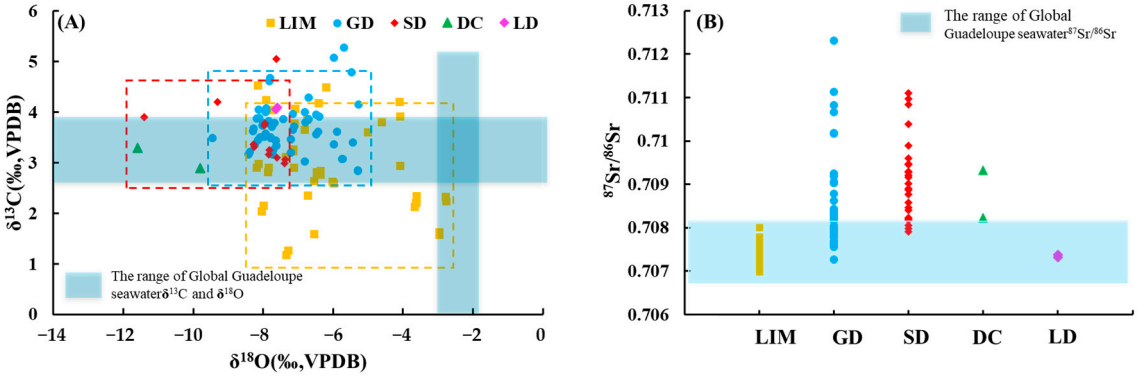

Figure 7. (**A**) Cross-plot of $\delta^{13}C$ versus $\delta^{18}O$ values of micritic bioclastic limestone (LIM), limy dolomite (LD), grain dolomite (GD), saddle dolomite (SD), dolomite cement (DC). The $\delta^{18}O$ values are negative in relation to the abnormal high geothermal temperature associated with the EMP. (**B**) $^{87}Sr/^{86}Sr$ ratio of LIM, LD, GD, SD, and DC. The $^{87}Sr/^{86}Sr$ ratio of GD is similar to that of LIM in some parts and similar to SD in others, and values of >0.712 represent the influence of meteoric water. Some of the data were obtained from previous research [18,21,22,102,103]. The global Permian $\delta^{13}C$, $\delta^{18}O$, and $^{87}Sr/^{86}Sr$ distribution range was obtained from Veizer [84].

5.2.2. Multiple Diagenetic Fluids

Affected by EMP activities, the early diagenetic stage of the Maokou Formation was influenced by various diagenetic fluids, such as seawater, meteoric water, and hydrothermal fluids. This study analyzed both the $^{87}Sr/^{86}Sr$ ratio and trace earth elements. It is generally agreed that carbonates with Mn/Sr < 1.5 did not experience significant diagenetic alteration [104,105]. In this respect, the Mn/Sr ratios of all LIM samples in this study were <0.35, indicating that the LIM samples had not undergone significant diagenetic alteration and that the ratios were related to the composition of ancient seawater. However, the Mn/Sr ratios of most GD samples were higher than those of the LIM but lower than 1.5, which suggested that they experienced minor diagenetic alteration (Table 1). The $^{87}Sr/^{86}Sr$ values

of LIM were similar to those of LD, and some GD values were distributed in the Permian seawater range (Figure 7B), indicating that the diagenetic fluid was mainly seawater. The REE patterns of LIM, LD, and of some GD samples were all characterized by enriched HREEs and negative Eu anomalies (Eu/Eu*: 0.84–0.90) (Figure 8A–C), which proves that seawater was the main diagenetic fluid. Abnormally high $^{87}Sr/^{86}Sr$ values similar to those of SD were found in some GD samples (Figure 7B). The REE patterns of these GD samples also exhibited rich HREE characteristics, but the patterns differed from those of LIM, LD, and others in that positive Eu anomalies were noted (Eu/Eu*: 1.03–1.5) (Figure 8D). This is an important characterization of the influence of hydrothermal fluids on diagenetic processes, and the diagenesis of these GD sample types was therefore influenced by hydrothermal fluids. The $^{87}Sr/^{86}Sr$ values of small amounts of GD were greater than 0.712 (Figure 7B), which signifies a meteoric water diagenetic environment. Moreover, significant karstification was observed in the study area, as detailed in Section 5.2.3, which indirectly proves the influence of meteoric water during diagenesis of the Maokou Formation.

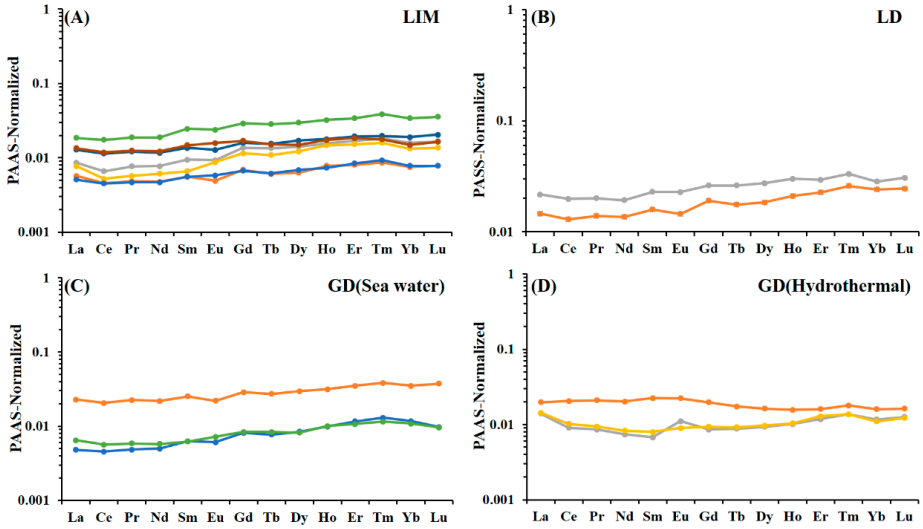

Figure 8. PAAS-normalized REE patterns of (**A**) micritic bioclastic limestone (LIM), (**B**) limy dolomite (LD), (**C**) grain dolomite (GD) (with negative Eu anomalies), and (**D**) grain dolomite (GD) (with positive Eu anomalies). The PAAS data were obtained from Taylor and Mclennan [77]. The REE patterns of LD and GD (sea water) are similar to those of LIM, with rich HREEs and negative Eu anomalies indicating the origin of sea water. The REE patterns of GD (hydrothermal) show positive Eu anomalies indicating the influence of hydrothermal fluid.

5.2.3. Karst and Fractures

Karstification is a pivotal factor in the genesis of reservoir spaces [106]; it serves as the main driver of secondary porosity and is a key enhancer of reservoir properties. In the core description and images obtained from the formation microimager (FMI), dissolution pores were seen to be developed (Figure 9A,B) as a result of uplift and dissolution occurring during the penecontemporaneous or shallow burial period. Section 5.2.2 showed that an $^{87}Sr/^{86}Sr$ value of GD was higher than 0.712 (Figure 7B), which provides evidence that Mbr 2 of the Maokou Formation experienced dissolution in meteoric water. The EMP activity resulted in stratigraphic uplift differences, and the karstification degree in HS2 and HS4 well cores were greater than that in HS6: both HS2 and HS4 are located on the slope of the NW-SE direction uplift zone, which was caused by EMP activity (Figure 3B), and the water energy in this area was extremely strong and karst pores were readily formed. This slope zone is also the main location of a high-energy particle shoal facies, where the intergranular pores between particles provided a material basis for karstification.

The FMI image showed that karst pores were accompanied by the development of fissures (Figure 9C). Under a polarizing microscope, fractures were observed to be widely

distributed and partially accompanied by dissolution pores, with CD, CAL, and asphalt filling the fracture and pore interiors (Figure 9D,E). Based on the different filling minerals observed, the filling process of cracks can be divided into three stages: CD is the earliest filling mineral; it has coarse and straight particles and is mainly distributed in the inner walls of cracks and pores. The second phase relates to asphalt filling between CD and CAL. CAL is the third filling mineral; it appears as red coarse crystalline calcite in the thin sections stained by Alizarin Red S and is distributed in the center of fractures and pores.

Karstification and fractures are the two most important factors resulting in the formation of secondary pores within the Maokou Formation. Against the background of EMP activities, karst was prone to occur within the slope zone, and dissolution pores are formed within it. With a relatively dense fracture distribution, the formation of large-scale fractures and porous reservoir systems is more likely to have occurred.

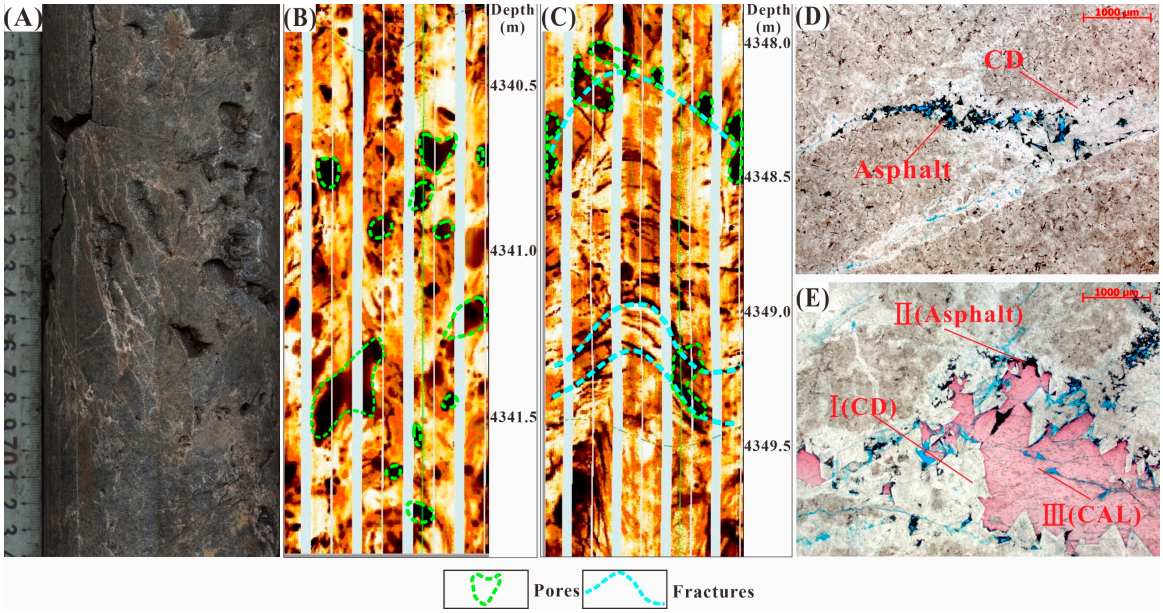

Figure 9. Abundant karst pores associated with fractures, proving that karstification is intense and fractures are the dominant channels within areas of karstification. (**A**) Core photograph of dissolved pores from well HS4 (4338.70–4338.94 m); (**B**) FMI image of dissolved pore from well HS4 (4340.5–4341.5 m); (**C**) FMI image of dissolved pores associated with fissures from well HS4 (4348–4349.5 m); (**D**) microphotograph of fractures filled with dolomite cement (DC) and asphalt in well HS4 (4339.25 m); (**E**) microphotograph of fractures and pores successively filled with dolomite cement (DC), asphalt, and calcite cement (CAL) in well HS4 (4339.53 m).

5.3. Model of Reservoir Genesis Associated with EMP Activity

Under the influence of EMP activity, significant changes occurred in the sedimentary environment and in the diagenesis of Maokou Formation reservoirs within the central Sichuan Basin. In this study, we established a genetic model for a reservoir within the Maokou Formation in central Sichuan that is based on the intensity and stage of EMP activity as follows: Stage 1: EMP activity began at the end of the sedimentary period of the Qixia Formation (Figure 10A). Stage 2: in the early stage of low-intensity EMP activity (from the end of the Qixia Formation to the depositional beginning of Mbr 2 of the Maokou Formation), the paleogeomorphology changed, and a NW-SE oriented uplift zone was formed; this resulted in the deposition of high-energy beach facies around the uplift zone (Figure 10B). Stage 3: during the continuous uplift stage of the EMP (the sedimentary stage from Mbr 2 to Mbr 4 of the Maokou Formation), the intensity of the stratigraphic uplift continued to increase, resulting in exposed dissolution and the formation of structural fractures (Figure 10C). Stage 4: with the increasing EMP activity (the period of intense uplift

after the deposition of Mbr 4 of the Maokou Formation), the maximum stratigraphic uplift, dissolution, and fracturing degrees were reached in the central Sichuan Basin (Figure 10D). The deposition of high-energy beach facies on an uplifted slope provided the foundation for the diagenetic transformation due to the presence of abundant intergranular pores. Seawater, hydrothermal fluid, and meteoric water jointly affected the early diagenesis of the reservoir and seawater, and hydrothermal fluids promoted dolomitization under high geothermal conditions. Meteoric water-controlled karstification mainly occurred on the uplifted slopes, and fractures were the dominant karst channels, leading to the relationship between fractures and karst pores.

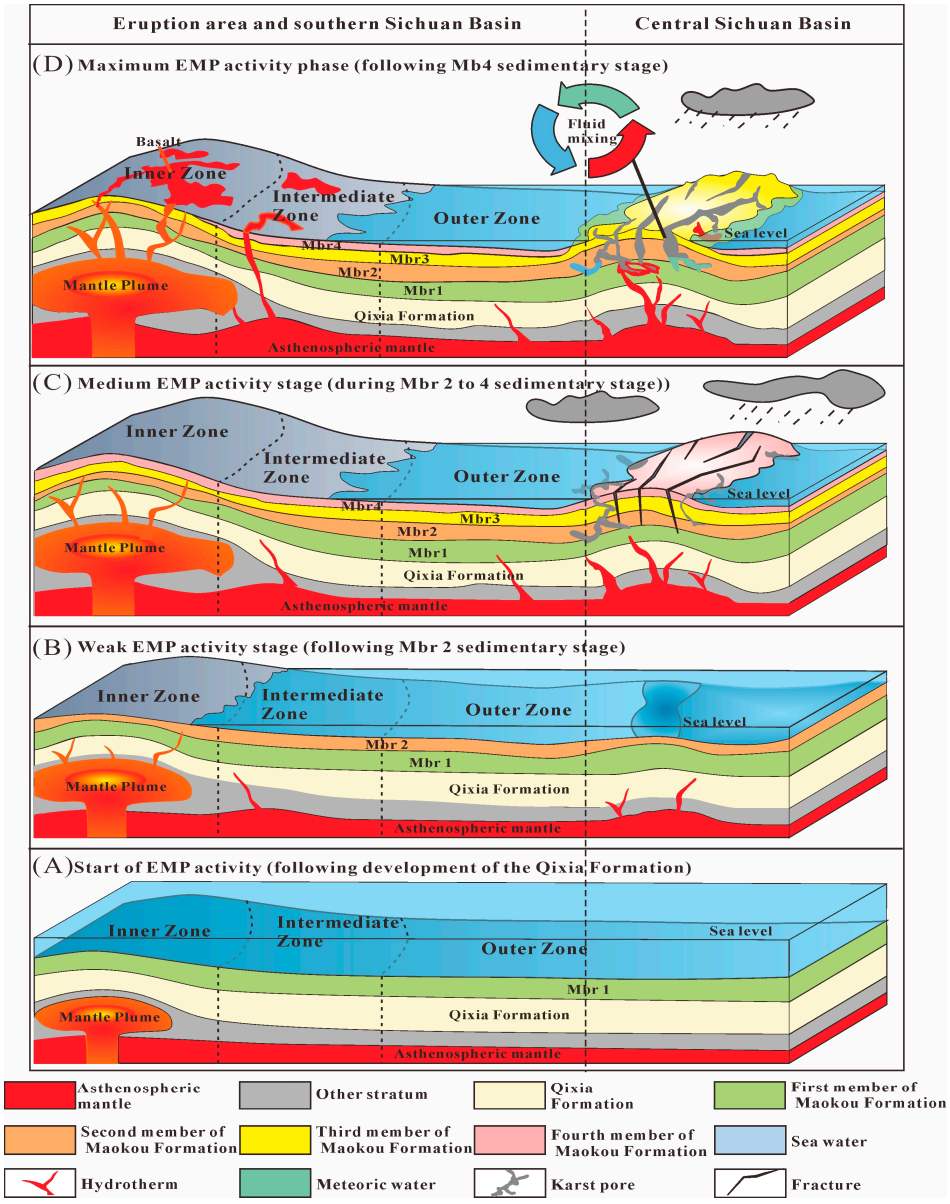

Figure 10. Reservoir genesis model of the Maokou Formation in the Sichuan Basin in association with the influence of EMP activity; (**A**) start of EMP activity following development of the Qixia Formation; (**B**) EMP activity leads to the formation of uplift zones, resulting in sedimentary differentiation in the second member of the Maokou Formation; (**C**) continuous EMP activity results in the generation of fractures and karst during the sedimentary stage from the second member to the fourth member of Maokou Formation; (**D**) during most intense EMP uplift period, which occurred following deposition of the fourth member of Maokou Formation, the karst was the strongest and accompanied by fractures.

6. Conclusions

This study focuses on the impact of Emeishan mantle plume activity on the genesis of the Maokou Formation reservoir. The sedimentation and early diagenesis stages of the Maokou Formation were accompanied by EMP activity, all of which had a significant impact on the genetic mechanisms of the reservoir. With respect to sedimentation, uplift from the EMP altered the paleogeomorphology of the area, and local uplift zones were formed in a NW–SE direction. High-energy beach facies developed on uplifted slopes, and these are the most advantageous sedimentary facies. GD is the main associated lithofacies, and its multiple intergranular pores provided the material basis for diagenetic transformation.

The diagenesis of the Maokou Formation was influenced by various fluids due to EMP activity, and these included seawater, hydrothermal fluids, and meteoric water. Furthermore, the dolomitization process of the Maokou Formation was influenced by both hydrothermal and seawater processes under a high geotherm. EMP activity provided a high geothermal temperature for the Maokou Formation, which resulted in extremely strong thermal fractionation and a strong negative $\delta^{18}O$ feature. The $^{87}Sr/^{86}Sr$ value range of GD was found to be relatively large and within the range of Permian seawater, but higher values similar to those of SD with a hydrothermal origin were also detected in GD samples. The REE patterns of GD also display two characteristic origins: seawater (enriched HREEs and negative Eu anomalies) and hydrothermal (enriched HREEs and negative Eu anomalies) origins. The continuous tectonic uplift of the EMP caused dissolution of the Maokou Formation via meteoric water leaching. Karstification occurs mainly on the slope of the uplift zone, which is also the location of high-energy beach facies. During the mantle plume uplift process, abundant fractures (karstification channels) were generated in the Maokou Formation. Based on the above evidence and results, we established a reservoir genetic model of the Maokou Formation in the central Sichuan Basin that shows the influence of EMP activity based on the associated intensity and stage.

The results of this study imply that large-scale fractured and porous reservoir systems were easily formed in the uplifted slope zone, and these contain abundant fractures. This study provides guidance for the exploration and development of carbonate gas reservoirs and provides reference for the study of mantle plume activity and carbonate reservoir genesis. However, there are shortcomings in the research on the process of diagenetic evolution in this study, which is the goal of the next step of this work.

Author Contributions: Conceptualization, Q.G. and X.L.; methodology, Q.G.; software, Z.G.; validation, Q.G., X.L. and L.Z.; formal analysis, M.Z. (Mao Zhu); investigation, M.Z. (Mengfei Zhou); resources, Y.H.; data curation, X.P.; writing—original draft preparation, Q.G.; writing—review and editing, H.Z.; visualization, S.D.; supervision, X.L., Y.W., W.L. and M.Y. All authors have read and agreed to the published version of the manuscript.

Funding: This study was jointly sponsored by the China National Petroleum Corporation's basic forward-looking major scientific and technological project (grant number 2021DJ1053).

Data Availability Statement: Due to the nature of this research, participants of this study did not agree for their data to be shared publicly.

Acknowledgments: The authors are grateful to the journal editor and the anonymous reviewers for their constructive comments. We also thank the Key Laboratory of Carbonate Reservoirs, China National Petroleum Corporation, Hangzhou, for their assistance with conducting $^{87}Sr/^{86}Sr$, $\delta^{13}C$, $\delta^{18}O$, and trace earth elements analyses.

Conflicts of Interest: We declare that we have no financial and personal relationships with other people or organizations that will inappropriately affect our work, and there are no professional or other personal interests of any nature or kind in any product, service and/or company that could be construed as influencing the position presented in, or the review of, the manuscript.

References

1. Li, X.Z.; Guo, Z.H.; Wan, Y.J.; Liu, X.H.; Zhang, M.L.; Xie, W.R.; Su, Y.H.; Hu, Y.; Feng, J.W.; Yang, B.X.; et al. Geological characteristics and development strategies for Cambrian Longwangmiao Formation gas reservoir in Anyue gas field, Sichuan Basin, SW China. *Pet. Explor. Dev.* **2017**, *44*, 398–406. [CrossRef]
2. Ma, X.H. A golden era for natural gas development in the Sichuan Basin. *Nat. Gas Ind.* **2017**, *37*, 1–10. [CrossRef]
3. Han, L.L.; Li, X.Z.; Liu, Z.Y.; Duan, G.F.; Wang, Y.J.; Guo, X.L.; Guo, W.; Cui, Y. Influencing factors and prevention measures of casing deformation in deep shale gas wells in Luzhou block, southern Sichuan Basin, SW China. *Pet. Explor. Dev.* **2023**, *50*, 979–988. [CrossRef]
4. Hu, A.P.; Pan, L.Y.; Hao, Y.; Shen, A.J.; Gu, M.F. Origin Characteristics and Distribution of Dolostone Reservoir in Qixia Formation and Maokou Formation, Sichuan Basin, China. *Mar. Orig. Pet. Geol.* **2018**, *23*, 39–52.
5. Duan, J.M.; Zheng, J.F.; Shen, A.J.; Zhu, M.; Yao, Q.Y.; Hao, Y. Characteristics and genesis of dolomite reservoir of the Lower Permian Qixia Formation in central Sichuan Basin. *Mar. Orig. Pet. Geol.* **2021**, *26*, 345–356.
6. Huang, S.P.; Jiang, Q.C.; Feng, Q.F.; Wu, Y.; Lu, W.H.; Su, W.; Chen, X.Y.; Ren, M.Y.; Peng, H. Type and distribution of Mid-Permian Maokou Formation karst reservoirs in southern Sichuan Basin, SW China. *Pet. Explor. Dev.* **2019**, *46*, 293–300. [CrossRef]
7. Li, R.; Su, C.P.; Shi, G.S.; Jia, H.F.; Li, S.H.; Yu, Y. The genesis of nodular limestone reservoirs of the first period of Maokou Formation of Permian in southern Sichuan Basin. *Nat. Gas Ind.* **2021**, *32*, 806–815.
8. Hu, S.; Tan, X.C.; Luo, B.; Zhang, B.J.; Zhang, Y.; Su, C.P.; Lu, F.F.; Li, M.L. Sequence stratigraphic characteristics and geological significance of the Permian Qixia Stage in northwestern Sichuan Basin. *J. Palaeogeogr.* **2020**, *20*, 1109–1126.
9. Hu, X.; Wang, Y.F.; Pei, S.Q.; Zeng, Q.; Li, R.R.; Long, H.Y.; Li, T.L.; Zhou, S.Y.; Sun, H.T. Sedimentary evolution and its influence on karst reservoir development of the Middle Permian Maokou Formation in the northwestern Sichuan Basin, China. *Nat. Gas Geosci.* **2022**, *33*, 572–587.
10. Zhao, W.Z.; Shen, A.J.; Hu, S.Y.; Zhang, B.M.; Pan, W.Q.; Zhou, J.G.; Wang, Z.C. Geological conditions and distributional features of large-scale carbonate reservoirs onshore China. *Pet. Explor. Dev.* **2012**, *39*, 1–12. [CrossRef]
11. Shen, A.J.; Zhao, W.Z.; Hu, A.P.; She, M.; Chen, Y.N.; Wang, X.F. Major factors controlling the development of marine carbonate reservoirs. *Pet. Explor. Dev.* **2015**, *42*, 545–554. [CrossRef]
12. Shen, A.J.; Chen, Y.N.; Meng, S.X.; Zheng, J.F.; Qiao, Z.F.; Ni, X.F.; Zhang, J.Y.; Wu, X.N. The research progress of marine carbonate reservoirs in China and its significance for oil and gas exploration. *Mar. Orig. Pet. Geol.* **2019**, *24*, 1–14.
13. Su, W.; Jiang, Q.C.; Chen, Z.Y.; Wang, Z.C.; Jiang, H.; Bian, C.S.; Feng, Q.F.; Wu, Y.L. Sequence stratigraphic features of Middle Permian Maokou Formation in the Sichuan Basin and their controls on source rocks and reservoirs. *Nat. Gas Ind.* **2015**, *35*, 34–43. [CrossRef]
14. Zhou, J.G.; Yao, G.S.; Yang, G.; Gu, M.F.; Yao, Q.Y.; Jiang, Q.C.; Yang, L.; Yang, Y.R. Lithofacies palaeogeography and favorable gas exploration zones of Qixia and Maokou Fms in the Sichuan Basin. *Nat. Gas Ind.* **2016**, *36*, 8–15.
15. Yang, Y.; Xie, J.R.; Zhao, L.Z.; Huang, P.H.; Zhang, X.H.; Chen, C.; Zhang, B.J.; Wen, L.; Wang, H.; Gao, Z.L.; et al. Breakthrough of natural gas exploration in the beach facies porous dolomite reservoir of Middle Permian Maokou Formation in the Sichuan Basin and its enlightenment: A case study of the tridimensional exploration of Well JT1 in the central-northern Sichuan Basin. *Nat. Gas Ind.* **2021**, *41*, 1–9.
16. Zhu, M.; Huang, S.W.; Song, X.; Wang, X.D.; Shi, J.B.; Tian, X.B.; Yao, Q.Y.; Wang, H. Main controlling factors of the Middle Permian dolomite reservoir and prediction of exploration zone in Tongnan-Hechuan block, Sichuan Basin. *China Pet. Explor.* **2022**, *27*, 149–161.
17. Jiang, Q.C.; Hu, S.Y.; Wang, Z.C.; Chi, Y.L.; Yang, Y.; Lu, W.H.; Wang, H.Z.; Li, Q.F. Paleokarst landform of the weathering crust of Middle Permian Maokou formation in Sichuan basin and selection of exporation regions. *Acta Pet. Sin.* **2012**, *33*, 949–960.
18. Liu, H.; Ma, T.; Tan, X.C.; Zeng, W.; Hu, G.; Xiao, D.; Luo, B.; Shan, S.J.; Su, C.P. Origin of structurally controlled hydrothermal dolomite in epigenetic karst system during shallow burial: An example from Middle Permian Maokou Formation, central Sichuan Basin, SW China. *Pet. Explor. Dev.* **2016**, *43*, 916–927. [CrossRef]
19. Zhang, Y.; Chen, S.L.; Zhang, X.L.; Zhang, X.H.; Xie, C.; Chen, C.; Yang, Y.R.; Gao, Z.L. Restoration of paleokarst geomorphology of Lower Permian Maokou Formation and its petroleum exploration implication in Sichuan Basin. *Lithol. Reserv.* **2020**, *32*, 44–55.
20. Bai, X.J.; Zheng, J.F.; Dai, K.; Hong, S.X.; Duan, J.M.; Liu, Y.M. Petrological, Geochemical and Chronological Characteristics of Dolomites in the Permian Maokou Formation and Constraints to the Reservoir Genesis, Central Sichuan Basin, China. *Minerals* **2023**, *13*, 1336. [CrossRef]
21. Chen, X.; Zhao, W.Z.; Zhang, L.P.; Zhao, Z.J.; Liu, Y.H.; Zhang, B.M.; Yang, Y. Discovery and exploration significance of structure-controlled hydrothermal dolomites in the Middle Permian of the central Sichuan basin. *Acta Pet. Sin.* **2012**, *33*, 562–569.
22. Jiang, Y.Q.; Gu, Y.F.; Li, K.H.; Li, S.; Luo, M.S.; He, B. Space types and origins of hydrothermal dolomite reservoirs in the Middle Permian strata, central Sichuan Basin. *Nat. Gas Ind.* **2018**, *38*, 16–24.
23. Ma, D.B.; Wang, Z.C.; Duan, S.F.; Gao, J.R.; Jiang, Q.C.; Jiang, H.; Zeng, F.Y.; Lu, W.H. Strike-slip faults and their significance for hydrocarbon accumulation in Gaoshiti–Moxi area, Sichuan Basin, SW China. *Pet. Explor. Dev.* **2018**, *45*, 795–805. [CrossRef]
24. Liu, J.Q.; Zheng, H.F.; Liu, B.; Liu, H.G.; Shi, K.B.; Guo, R.T.; Zhang, X.F. Characteristics and genetic mechanism of the dolomite in the Middle Permian Maokou Formation, central Sichuan area. *Acta Pet. Sin.* **2017**, *38*, 386–398.
25. Wang, Z.C.; Jiang, Q.C.; Huang, S.P.; Zhou, H.; Feng, Q.F.; Dai, X.F.; Lu, W.H.; Ren, M.Y. Geological conditions for massive accumulation of natural gas in the Mid-Permian Maokou Fm of the Sichuan Basin. *Nat. Gas Ind.* **2018**, *38*, 30–38.

26. Zhang, Y.; Cao, Q.G.; Luo, K.P.; Li, L.L.; Liu, J.L. Reservoir exploration of the Permian Maokou Formation in the Sichuan Basin and enlightenment obtained. *Oil Gas Geol.* **2022**, *43*, 610–620.
27. Chung, S.L.; Jahn, B.M. Plume-lithosphere interaction in generation of the Emeishan flood basalts at the Permian-Triassic boundary. *Geology* **1995**, *23*, 889. [CrossRef]
28. Courtillot, V.; Jaupart, C.; Manighetti, I. On causal links between flood basalts and continental breakup. *Earth Planet. Sci. Lett.* **1999**, *166*, 177–195. [CrossRef]
29. Cohen, K.M.; Finney, S.M.; Gibbard, P.L.; Fan, J. The ICS International Chronostratigraphic Chart. *Episodes* **2013**, *36*, 199–204. [CrossRef] [PubMed]
30. Xu, Y.G.; He, B.; Chung, S.L.; Menzies, M.A.; Frey, F.A. Geologic, geochemical, and geophysical consequences of plume involvement in the Emeishan flood-basalt province. *Geology* **2004**, *32*, 917–920. [CrossRef]
31. He, B.; Xu, Y.G.; Guan, J.P.; Zhong, Y.T. Paleokarst on the top of the Maokou Formation: Further evidence for domal crustal uplift prior to the Emeishan flood volcanism. *Lithos* **2010**, *119*, 1–9. [CrossRef]
32. Shi, Z.; Li, W.; Luo, Q.; Zhang, J.; Wang, Y.; Tian, Y.; Yin, G. Emeishan mantle plume activity and carbon isotope responses in the Middle Permian, South China. *J. Asian Earth Sci.* **2019**, *189*, 104145. [CrossRef]
33. Zhao, W.Z.; Zhang, G.Y.; Wang, H.J.; Wang, S.J.; Wang, Z.C. Basic features of petroleum geology in the superimposed petroliferous basins of China and their research methodologies. *Pet. Explor. Dev.* **2003**, *2*, 1–8. [CrossRef]
34. Pang, X.; Zhou, X.; Jiang, Z. Hydrocarbon Reservoirs Formation, Evolution, Prediction and Evaluation in the Superimposed Basins. *Acta Geol. Sin.* **2012**, *86*, 1–103.
35. Liu, S.G.; Sun, W.; Zhong, Y.; Deng, B.; Song, J.M.; Ran, B.; Luo, Z.L.; Han, K.Y.; Company, G.F. Evolutionary episodes and their characteristics within the Sichuan marine craton basin during Phanerozoic Eon, China. *Acta Petrol. Sin.* **2017**, *33*, 1058–1072.
36. Wei, G.Q.; Wang, Z.H.; Li, J.; Yang, W.; Xie, Z.Y. Characteristics of source rocks, resource potential and exploration direction of Sinian and Cambrian in Sichuan Basin. *Nat. Gas Geosci.* **2017**, *2*, 289–302. [CrossRef]
37. Wang, Z.C.; Zhao, W.Z.; Peng, H.Y. Characteristics of multi-source petroleum systems in Sichuan basin. *Pet. Explor. Dev.* **2002**, *29*, 26–29.
38. Zhou, M.F.; Malpas, J.G.; Son, X.Y.; Robinson, P.T.; Sun, M.; Kennedy, A. A temporal link between the Emeishan Large Igneous Province (SW China) and the end-Guadalupian mass extinction. *Earth Planet. Sci. Lett.* **2002**, *196*, 113–122. [CrossRef]
39. He, B.; Xu, Y.G.; Huang, X.L.; Luo, Z.Y.; Shi, Y.R.; Yang, Q.J.; Yu, S.Y. Age and duration of the Emeishan flood volcanism, SW China: Geochemistry and SHRIMP zircon U–Pb dating of silicic ignimbrites, post-volcanic Xuanwei Formation and clay tuff at the Chaotian section. *Earth Planet. Sci. Lett.* **2007**, *255*, 306–323. [CrossRef]
40. Shellnutt, J.G.; Usuki, T.; Kennedy, A.K.; Chiu, H.Y. A lower crust origin of some flood basalts of the Emeishan large igneous province, SW China. *J. Asian Earth Sci.* **2015**, *109*, 74–85. [CrossRef]
41. Hei, H.X.; Su, S.G.; Wang, Y.; Mo, X.X.; Luo, Z.H.; Liu, W.G. Rhyolites in the Emeishan large igneous province (SW China) with implications for plume-related felsic magmatism. *J. Asian Earth Sci.* **2018**, *164*, 344–365. [CrossRef]
42. Li, H.; Zhang, Z.; Santosh, M.; Linsu, L.; Han, L.; Liu, W. Late Permian basalts in the Yanghe area, eastern Sichuan Province, SW China: Implications for the geodynamics of the Emeishan flood basalt province and Permian global mass extinction. *J. Asian Earth Sci.* **2017**, *134*, 293–308. [CrossRef]
43. Xu, Y.; Chung, S.L.; Jahn, B.M.; Wu, G. Petrologic and geochemical constraints on the petrogenesis of Permian–Triassic Emeishan flood basalts in southwestern China. *Lithos* **2001**, *58*, 145–168. [CrossRef]
44. Shellnutt, J.G. The Emeishan large igneous province: A synthesis. *Geosci. Front.* **2014**, *5*, 369–394. [CrossRef]
45. Li, H.B.; Zhang, Z.C.; Richard, E. Giant radiating mafic dyke swarm of the Emeishan Large Igneous Province: Identifying the mantle plume centre. *Terra Nova* **2015**, *27*, 247–257. [CrossRef]
46. Zhou, M.F.; Wang, Z.C.; Zhao, W.W.; Qi, L.; Zhao, Z.; Zhou, J.; Huang, Z.; Chen, W.T. A reconnaissance study of potentially important scandium deposits associated with carbonatite and alkaline igneous complexes of the Permian Emeishan Large Igneous Province, SW China. *J. Asian Earth Sci.* **2022**, *236*, 105309. [CrossRef]
47. Xiao, L.; Xu, Y.G.; Chung, S.L.; He, B.; Mei, H.J. Chemostratigraphic Correlation of Upper Permian Lavas from Yunnan Province, China: Extent of the Emeishan Large Igneous Province. *Int. Geol. Rev.* **2003**, *45*, 753–766. [CrossRef]
48. Xu, J.F.; Suzuki, K.; Xu, Y.G.; Mei, H.J.; Jie, L. Os, Pb, and Nd isotope geochemistry of the Permian Emeishan continental flood basalts: Insights into the source of a large igneous province. *Geochim. Et Cosmochim. Acta* **2007**, *71*, 2104–2119. [CrossRef]
49. Ganino, C.; Arndt, N.T. Climate changes caused by degassing of sediments during the emplacement of large igneous provinces. *Geology* **2010**, *37*, 323–326. [CrossRef]
50. Huang, H.; Huyskens, M.H.; Yin, Q.Z.; Cawood, P.A.; Hou, M.; Yang, J.; Xiong, F.; Du, Y.; Yang, C. Eruptive tempo of Emeishan large igneous province, southwestern China and northern Vietnam: Relations to biotic crises and paleoclimate changes around the Guadalupian-Lopingian boundary. *Geology* **2022**, *50*, 1083–1087. [CrossRef]
51. Wignall, P.B. Large igneous provinces and mass extinctions. *Earth Sci. Rev.* **2001**, *53*, 1–33. [CrossRef]
52. Knoll, A.H.; Bambach, R.K.; Payne, J.L.; Pruss, S.; Fischer, W.W. Paleophysiology and end-Permian mass extinction. *Earth Planet. Sci. Lett.* **2007**, *256*, 295–313. [CrossRef]
53. Ogden, D.E.; Sleep, N.H. Explosive eruption of coal and basalt and the end-Permian mass extinction. *Proc. Natl. Acad. Sci. USA* **2012**, *109*, 59–62. [CrossRef]

54. Penn, J.L.; Deutsch, C.; Payne, J.L.; Sperling, E.A. Temperature-dependent hypoxia explains biogeography and severity of end-Permian marine mass extinction. *Science* **2018**, *362*, aat1327. [CrossRef] [PubMed]
55. Cribb, A.T.; Bottjer, D.J. Complex marine bioturbation ecosystem engineering behaviors persisted in the wake of the end-Permian mass extinction. *Sci. Rep.* **2020**, *10*, 203. [CrossRef]
56. Zhang, Z. Geochemistry of Picritic and Associated Basalt Flows of the Western Emeishan Flood Basalt Province. *China J. Petrol.* **2006**, *47*, 1997–2019. [CrossRef]
57. Zhang, Z.; Zhi, X.; Lei, C.; Saunders, A.D.; Reichow, M.K. Re–Os isotopic compositions of picrites from the Emeishan flood basalt province, China. *Earth Planet. Sci. Lett.* **2008**, *276*, 30–39. [CrossRef]
58. Meng, F.; Tian, Y.; Kerr, A.C.; Wu, Z.; Xu, Q.; Du, Q.; Zhou, Y.; Liu, J. Geochemistry and petrogenesis of Late Permian basalts from the Sichuan Basin, SW China: Implications for the geodynamics of the Emeishan mantle plume. *J. Asian Earth Sci.* **2023**, *241*, 105477. [CrossRef]
59. Cox, K.G. The role of mantle plumes in the development of continental drainage patterns. *Nature* **1989**, *342*, 873–877. [CrossRef]
60. Campbell, I.H.; Griffiths, R.W. Implications of mantle plume structure for the evolution of flood basalts. *Earth Planet. Sci. Lett.* **1990**, *99*, 79–93. [CrossRef]
61. Campbell, I.H. Large Igneous Provinces and the Mantle Plume Hypothesis. *Elements* **2005**, *1*, 265–269. [CrossRef]
62. Sleep, N.H. Mantle plumes from top to bottom. *Earth-Sci. Rev.* **2006**, *77*, 231–271. [CrossRef]
63. Bryan, S.E.; Ernst, R.E. Revised definition of Large Igneous Provinces (LIPs). *Earth Sci. Rev.* **2008**, *86*, 175–202. [CrossRef]
64. He, B.; Xu, Y.G.; Chung, S.L.; Long, X.; Wang, Y. Sedimentary evidence for a rapid, kilometer-scale crustal doming prior to the eruption of the Emeishan flood basalts. *Earth Planet. Sci. Lett.* **2003**, *213*, 391–405. [CrossRef]
65. Li, S.G. Variscan orogeny of the southeast of China. *Bull. Geol. Soc. China* **1931**, *11*, 200–217.
66. He, B.; Xu, Y.G.; Wang, Y.M.; Xiao, L. Nature of the Dongwu Movement and Its Temporal and Spatial Evolution. *Earth Sci.* **2005**, *30*, 89–96.
67. Chang, W.Y.; Sun, T.C.; Wu, L.P. Stratigraphic unconformity in Kuangsi. *Bull. Geol. Soc. China* **1941**, *21*, 131–156. [CrossRef]
68. Hu, H.T. Discussing the horizon of the Mingshan formation in the South of Anhui Province and the crustal variation between the Lower and Upper Permian. *Geol. Rev.* **1951**, *6*, 25–31.
69. Hu, S.Z. Discussion on the boundary problem between the Upper and Lower Permian in South China. *Chin. Geol.* **1986**, *12*, 14–16.
70. Hu, S.Z. On the event of Dongwu Movement and its relation with Permian subclassification. *J. Stratigr.* **1994**, *18*, 309–315.
71. Feng, S.N. New knowledge on Dongwu movement. *Geoscience* **1991**, *5*, 378–384.
72. Li, X.B.; Zeng, X.W.; Wang, C.S.; Liu, A.; Bai, Y.S. Sedimentary response to the Dongwu movement: A case of the unconformity on top of the Permian Maokou Fm in the western Hubei-Hunan and neighboring areas. *J. Stratigr.* **2011**, *35*, 299–304.
73. Su, W.; Hu, S.Y.; Jiang, Q.C.; Zhang, J.; Ren, M.Y. Sedimentary responses to the Dongwu movement and the influence of the Emeishan mantle plume in Sichuan Basin, Southwest China: Significance for petroleum geology. *Carbonates Evaporites* **2020**, *35*, 108. [CrossRef]
74. Zhao, Z.J.; Zhou, H.; Chen, X.; Liu, Y.H.; Zhang, Y.B.; Liu, Y.E.; Yang, Y. Sequence lithofacies paleogeography and favorable exploration zones of the Permian in Sichuan Basin and adjacent areas. *Acta Pet. Sin.* **2012**, *33* (Suppl. S2), 35–51.
75. Wang, Y.; Jin, Y. Permian palaeogeographic evolution of the jiangnan basin, South China. *Palaeogeogr. Palaeoclimatol. Palaeoecol.* **2000**, *160*, 35–44.
76. Brigaud, B.; Durlet, C.; Deconinck, J.F.; Vincent, B.; Thierry, J.; Trouiller, A. The origin and timing of multiphase cementa-tion in carbonates: Impact of regional scale geodynamic events on the Middle Jurassic Limestones diagenesis (Paris Basin, France). *Sediment. Geol.* **2009**, *222*, 161–180. [CrossRef]
77. Taylor, S.R.; Mclennan, S.M. The continental crust: Its composition and evolution. *J. Geol.* **1985**, *94*, 57–72.
78. Webb, G.E.; Kamber, B.C. Rare earth elements in Holocene reefal microbialites: A new shallow seawater proxy. *Geochim. Et Cosmochim. Acta* **2000**, *64*, S0016–S703700400. [CrossRef]
79. German, C.R.; Elderfield, H. Application of the Ce anomaly as a paleoredox indicator: The ground rules. *Paleoceanography* **1990**, *5*, 823–833. [CrossRef]
80. Bolhar, R.; Van Kranendonk, M.J. A non-marine depositional setting for the northern Fortescue Group, Pilbara Craton, inferred from trace element geochemistry of stromatolitic carbonates. *Precambrian Res.* **2007**, *155*, 229–250. [CrossRef]
81. Kamber, B.S.; Webb, G.E. The geochemistry of late Archaean microbial carbonate: Implications for ocean chemistry and continental erosion history. *Geochim. Et Cosmochim. Acta* **2001**, *65*, 2509–2525. [CrossRef]
82. Shields, G.A.; Webb, G.E. Has the REE composition of seawater changed over geological time? *Chem. Geol.* **2004**, *204*, 103–107. [CrossRef]
83. Michard, A.; Albarede, F. The REE content of some hydrothermal fluids. *Chem. Geol.* **1986**, *55*, 51–60. [CrossRef]
84. Veizer, J.; Ala, D.; Azmy, K.; Bruckschen, P.; Buhl, D.; Bruhn, F.; Carden, G.A.F.; Diener, A.; Stefan, E.; Godderis, Y.; et al. $^{87}Sr/^{86}Sr$, $\delta^{13}C$ and $\delta^{18}O$ evolution of Phanerozoic seawater. *Chem. Geol.* **1999**, *161*, 59–88.
85. Sengor, A.M.C. Elevation as indicator of mantle-plume activity. *Spec. Pap. Geol. Soc. Am.* **2001**, *352*, 183–225.
86. Campbell, I.H. Testing the plume theory. *Chem. Geol.* **2007**, *241*, 153–176. [CrossRef]
87. Guo, Z.J.; Zhu, B.; Du, W.; Liu, R.C.; Liu, D.D. No pre-eruptive uplift in the Emeishan large igneous province: New evidences from its 'inner zone', Dali area, Southwest China. *J. Volcanol. Geotherm. Res.* **2014**, *269*, 57–67. [CrossRef]

88. Jerram, D.A.; Widdowson, M.; Wignall, P.B.; Sun, Y.D.; Lai, X.L.; Bond, D.P.G.; Torsvik, T.H. Submarine palaeoenvironments during Emeishan flood basalt volcanism, SW China: Implications for plume-lithosphere interaction during the Capitanian, Middle Permian ('end Guadalupian') extinction event. *Palaeogeogr. Palaeoclimatol. Palaeoecol. Int. J. Geo-Sci.* **2016**, *441*, 65–73. [CrossRef]
89. Sheth, H.C. Flood basalts and large igneous provinces from deep mantle plumes: Fact, fiction, and fallacy. *Tectonophysics* **1999**, *311*, 1–29. [CrossRef]
90. Saunders, A.D.; Jones, S.M.; Morgan, L.A.; Pierce, K.L.; Widdowson, M.; Xu, Y.G. Regional uplift associated with continental large igneous provinces: The roles of mantle plumes and the lithosphere. *Chem. Geol.* **2007**, *241*, 282–318. [CrossRef]
91. Xu, Y.G.; Luo, Z.Y.; Huang, X.L.; He, B.; Xiao, L.; Xie, L.W.; Shi, Y.R. Zircon U–Pb and Hf isotope constraints on crustal melting associated with the Emeishan mantle plume. *Geochim. Et Cosmochim. Acta* **2008**, *72*, 3084–3104. [CrossRef]
92. Sobolev, S.S.; Alexander, V.S.; Dmitry, V.K.; Nadezhda, A.K.; Alexey, G.P.; Nicholas, T.A.; Viktor, A.R.; Yuri, R.V. Linking mantle plumes, large igneous provinces and environmental catastrophes. *Nature* **2011**, *477*, 312–316. [CrossRef] [PubMed]
93. Gaschnig, R.M.; Vervoort, J.D.; Lewis, R.S.; Tikoff, B. Probing for Proterozoic and Archean crust in the northern U.S. Cordillera with inherited zircon from the Idaho batholith. *Geol. Soc. Am. Bull.* **2013**, *125*, 73–88. [CrossRef]
94. Mitchell, N.A.; Yanites, B.J. Spatially Variable Increase in Rock Uplift in the Northern U.S. Cordillera Recorded in the Distribution of River Knickpoints and Incision Depths. *J. Geophys. Res. Earth Surf.* **2019**, *124*, 1238–1260. [CrossRef]
95. Davies, G.F.; Richards, M.A. Mantle convection. *J. Geol.* **1992**, *100*, 151–206. [CrossRef]
96. Hill, R.I. Mantle plumes and continental tectonics. *Lithos* **1993**, *30*, 193–206. [CrossRef]
97. Loper, D.E.; Stacey, F.D. The dynamical and thermal structure of deep mantle plumes. *Phys. Earth Planet. Inter.* **1983**, *33*, 304–317. [CrossRef]
98. Hofmann, F.A.W. Dynamics and internal structure of a lower mantle plume conduit. *Earth Planet. Sci. Lett.* **2009**, *100*, 151–206. [CrossRef]
99. Ali, J.; Fitton, J.; Herzberg, C. Emeishan large igneous province (SW China) and the mantle plume up-doming hypothesis. *J. Geol. Soc.* **2010**, *167*, 953–959. [CrossRef]
100. Zhu, C.Q.; Xu, M.; Yuan, Y.S.; Zhao, Y.Q.; Shan, J.N. Palaeogeothermal response and record of the effusing of Emeishan basalts in the Sichuan basin. *Chin. Sci. Bull.* **2010**, *55*, 949–956. [CrossRef]
101. Zhu, C.Q.; Hu, S.B.; Qiu, N.S.; Jiang, Q.; Rao, S.; Liu, S. Geothermal constraints on Emeishan mantle plume magmatism: Paleotemperature reconstruction of the Sichuan Basin, SW China. *Int. J. Earth Sci.* **2016**, *107*, 71–88. [CrossRef]
102. Li, T.; Zhu, D.C.; Yang, M.L.; Li, P.P.; Zou, Y.H. Influence of hydrothermal activity on the Maokou Formation dolostone in the central and western Sichuan Basin. *Oil Gas Geol.* **2021**, *42*, 639–651. [CrossRef]
103. Li, S.J.; Yang, T.B.; Han, Y.Q.; Gao, P.; Wo, Y.J.; He, Z.L. Hydrothermal dolomitization and its role in improving Middle Permian reservoirs for hydrocarbon accumulation, Sichuan Basin. *Oil Gas Geol.* **2021**, *42*, 1265–1280.
104. Fölling, P.G.; Frimmel, H.E. Chemostratigraphic correlation of carbonate successions in the Gariep and Saldania Belts, Namibia and South Afric. *Basin Res.* **2002**, *14*, 69–88. [CrossRef]
105. Motte, G.; Hoareau, G.; Callot, J.P.; R'evillon, S.; Piccoli, F.; Calassou, S.; Gaucher, E.C. Rift and salt-related multi-phase dolo-mitization: Example from the northwestern Pyrenees. *Mar. Pet. Geol.* **2021**, *126*, 104932. [CrossRef]
106. Tian, X.S.; Shi, Z.J.; Yin, G.; Wang, Y.; Tan, Q. Carbonate diagenetic products and processes from various diagenetic environ-ments in Permian paleokarst reservoirs: A case study of the limestone strata of Maokou formation in Sichuan Basin, South China. *Carbonates Evaporites* **2017**, *32*, 15–230. [CrossRef]